Applied Physics Letters

Birefringence of orthorhombic $DyScO_3$: Toward a terahertz quarter-wave plate

Cite as: Appl. Phys. Lett. **118**, 223506 (2021); https://doi.org/10.1063/5.0043216
Submitted: 07 January 2021 • Accepted: 11 May 2021 • Published Online: 04 June 2021

Chia-Jung Yang, Jingwen Li, Jannis Lehmann, et al.

Applied Physics Letters ARTICLE scitation.org/journal/apl

Birefringence of orthorhombic $DyScO_3$: Toward a terahertz quarter-wave plate

Cite as: Appl. Phys. Lett. **118**, 223506 (2021); doi: 10.1063/5.0043216
Submitted: 7 January 2021 · Accepted: 11 May 2021 ·
Published Online: 4 June 2021

Chia-Jung Yang,[1,a)] Jingwen Li,[1] Jannis Lehmann,[1] Nives Strkalj,[1] Morgan Trassin,[1] Manfred Fiebig,[1,a)] and Shovon Pal[1,2,a)]

AFFILIATIONS

[1]Department of Materials, ETH Zurich, 8093 Zurich, Switzerland
[2]School of Physical Sciences, National Institute of Science Education and Research, HBNI, Jatni 752 050 Odisha, India

[a)]**Authors to whom correspondence should be addressed:** chia-jung.yang@mat.ethz.ch, manfred.fiebig@mat.ethz.ch, and shovon.pal@niser.ac.in

ABSTRACT

With growing interest in exploring fundamental phenomena at terahertz (THz) frequencies, the need for controlling the polarization state of THz radiation is indispensable. However, simple optical elements, such as waveplates that allow creating circularly-polarized THz radiation, are scarce. Here, we present THz quarter-wave plates (QWPs) made out of (110)-cut and (001)-cut $DyScO_3$ (DSO) crystals. We examine the complex refractive indices along the in-plane axes and map the birefringence of both DSO crystals. Further, we demonstrate that both 50-μm-thick (110)-cut DSO and 370-μm-thick (001)-cut DSO crystals behave like a QWP over a broad frequency range of 0.50–0.70 THz and 0.50–0.61 THz, respectively, with a phase tolerance of $\pm 3\%$.

The so-called terahertz ($1\,\text{THz} = 10^{12}\,\text{Hz}$) frequency range of the electromagnetic spectrum spans from 0.1 to 10 THz. This spectral range has remained unexplored for a long time due to the lack of intense radiation sources and sensitive detectors. Over the past few decades, extensive progress has been made toward the development and application of THz technology.[1–3] In particular, these include intense single-cycle THz pulse generation[4–7] and THz time-domain spectroscopy (THz-TDS).[8–11] From the fundamental point of view, light-matter interaction in this range is an ideal tool for studying collective excitations in solid-state systems, such as phonons,[12] magnons,[13] and heavy fermions.[14–16] In addition, the non-destructive nature of THz radiation makes it ideal for investigating the dynamic properties (conductivity, dielectric function, etc.) in a contactless manner in thin films[17,18] where mechanical contacts are detrimental. Recently, THz-TDS has been used to investigate soft vibrational modes in thin ferroelectric $SrTiO_3$[19] and $PbTiO_3$[20] films, and the non-Fermi-liquid behavior in thin films of heavy-fermion material, $YbRh_2Si_2$.[21] While these investigations can be performed using linearly-polarized (LP) THz light, there are certain phenomena where the helicity inherent for circularly-polarized (CP) THz light is indispensable, such as in measuring circular dichroism,[22] the quasi-particle Hall-effect in superconductors,[23] ionization of Rydberg atoms,[24] generation of nanoscopic toroidal moments,[25] etc. In addition, CP THz light is of great importance for investigating chiral structures in bio-molecules with promising applications, such as drug delivery and biological sensing.[1,26]

Quarter-wave plates (QWPs) for generating CP THz light can be designed in different ways, such as *form* birefringence, liquid crystals, and the intrinsic crystal anisotropy. *Form* birefringence, based on an anisotropic periodic structure, can be induced in artificial manners using gratings, stack of papers,[27] or Pancharatnam–Berry metasurfaces.[28,29] Optical elements that incorporate liquid crystals offer an electrically tunable birefringence.[30] These devices are, however, bulky and complex to fabricate. Commercially available THz QWPs are mostly based on the intrinsic crystal anisotropy of quartz, which has a high transmittance in the THz range[31] and exhibits a strong birefringence. The narrow bandwidth of a single quartz-based QWP ($\approx$63 GHz,[32] within $\pm 3\%$ tolerance) is not suitable for applications in THz-TDS. To obtain broadband operation ($\approx$1 THz), special designs[32] are required where, for example, multiple quartz plates have to be precisely adjusted in thickness and stacked together with proper orientations. Hence, there is a need for identifying new materials that combine robust and broadband operation with a simple fabrication process. Since many materials are not transparent to THz radiation, the choices are very limited. Among the few options, orthorhombic

DSO crystals exhibit high potential with a reasonable THz transmittance.[33,34] Furthermore, both (110)-cut and (001)-cut DSO crystals are frequently used as substrates for growing various thin film heterostructures,[35–37] extending the possibility toward integrated device architectures that requires CP THz light. To our surprise, the birefringence of DSO in the THz range appears to have remained unexplored so far. To our advantage, however, measurement techniques to access the polarization state of the THz light are abundant both in the frequency domain[38–41] and in the time domain.[32,42–45]

In this Letter, we investigate and utilize the optical properties of (110)-cut and (001)-cut DSO crystals at THz frequencies. We use phase-sensitive THz-TDS to determine the complex refractive indices along different crystallographic axes. We then employ a THz polarimetry technique similar to Ref. 32 that allows us to precisely determine the phase retardation and the polarization of the transmitted THz radiation. We show that, unlike quartz (with $\Delta\omega/\omega = 0.07$, $\Delta\omega$ is the working frequency range and ω is the mean of the frequency range), a single 50-μm-thick (110)-cut DSO crystal or a single 370-μm-thick (001)-cut DSO crystal behaves like a QWP over a frequency range as broad as 0.50–0.70 THz ($\Delta\omega/\omega = 0.33$) or 0.50–0.61 THz ($\Delta\omega/\omega = 0.19$), respectively, with a phase tolerance of $\pm 3\%$. This provides a beneficial and simpler setting for designing waveplates for a relatively broader THz frequency range. With a careful design combining different orientations and surface cuts of DSO, there is even room for improvement of the bandwidth.

In our experiment, we generate single-cycle linearly-polarized THz pulses with a pulse energy of a few nanojoules by optical rectification in a 0.5-mm-thick (110)-cut ZnTe single-crystal, using 90% of an amplified Ti:Sapphire laser output (wavelength 800 nm, pulse duration 50 fs, pulse repetition rate 1 kHz, 2.5 mJ pulse energy).[46] The residual 10% of the laser output is used for electro-optic sampling of the transmitted THz wave. The THz and the infrared beams are collinearly focused onto a 0.5-mm-thick (110)-cut ZnTe detection crystal. The THz-induced ellipticity of the sampling light beam is measured using a QWP, a Wollaston prism, and a balanced photodiode. The signal from the balanced photodiode is analyzed with a lock-in amplifier. In order to increase the accessible time delay between the THz and the probe pulses, Fabry–Pérot resonances from the faces of the detection crystal are suppressed by a 2-mm-thick, THz-inactive (100)-cut ZnTe crystal that is optically bonded to the back of the detection crystal.

We fabricate our samples from (110)-cut and (001)-cut DSO crystals, supplied by *Crystec GmbH*. While the (110)-cut DSO is thinned down to $50 \pm 3\,\mu$m, and the (001)-cut DSO is thinned down to $370 \pm 5\,\mu$m. Both samples are then polished to obtain optically flat surfaces. The choice of thickness and cuts is defined by the birefringence and the fact that the design is for a zero-order QWP-like performance. At first, we measure the birefringence of both DSO crystals in a standard transmission-mode THz-TDS setup. We orient the DSO crystals and find that the maximum transmitted signal for the (110)-cut DSO is when the electric field of THz (E_{THz}) is parallel to the crystallographic [1$\bar{1}$0] axis, while for the (001)-cut DSO, the E_{THz} is parallel to the crystallographic [100] axis. We then rotate the DSO crystals in the sample plane by 90° and obtain the transients along the other orthogonal in-plane axes, i.e., the crystallographic [001] axis for the (110)-cut DSO and [010] axis for the (001)-cut DSO crystal. The transmitted THz electric fields in the time domain are shown in Figs. 1(a) and 1(b). All signals are normalized to the maximum field value

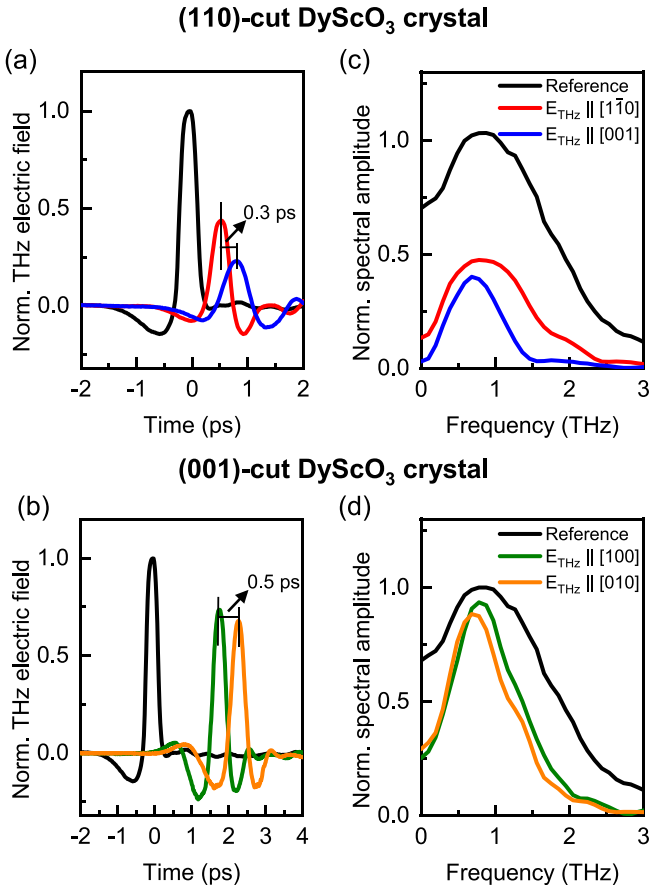

FIG. 1. The transmitted THz signals along (a) [1$\bar{1}$0] and [001] and (b) [100] and [010] in-plane crystallographic axes of the (110)-cut and (001)-cut DSO crystal, respectively. All the time transients are normalized to the reference signal. The spectra obtained by Fourier transformation along (c) [1$\bar{1}$0] and [001] and (d) [100] and [010] in-plane crystallographic axes.

of the reference (air). We can see from Fig. 1(a) that the THz transient along [1$\bar{1}$0] is shifted by ≈0.3 ps in time with respect to the one along [001], while in Fig. 1(b), the THz transient along [110] is shifted by ≈0.5 ps with respect to the one along [010]. These observations point toward a strong birefringence of the two in-plane orthogonal axes for both DSO crystals. The corresponding Fourier-transformed (FT) spectra are shown in Figs. 1(c) and 1(d). The transmittances along the [1$\bar{1}$0], [001], [100], and [001] directions are 50%, 25%, 67%, and 57%, respectively. The amplitude differences of the transmitted radiation along the different crystallographic directions are in fact a combination of both Fresnel reflection losses at the surface and the absorption loss inside the crystals.

To quantify and make use of this birefringence, we determine the refractive indices along the two in-plane axes [1$\bar{1}$0], [001] for the (110)-cut DSO and along [100], [010] for the (001)-cut DSO. When an in-plane crystallographic axis of the DSO crystal is oriented parallel to the electric field of linearly-polarized THz radiation, the transmitted beam carries information on many optical parameters along that specific crystallographic direction. These optical parameters include the

refractive index n, extinction coefficient κ, and the absorption coefficient α. To extract these parameters, the respective THz signals in the time domain are converted to the corresponding spectra in the frequency domain by Fourier transformation. Normalizing the sample spectrum with the reference spectrum yields the complex-valued transfer function. All optical parameters can then be obtained from the logarithm of the amplitude and the phase of the transfer function[47] (see Sec. II of the supplementary material for more details).

The frequency-dependent refractive indices and the extinction coefficients along [1$\bar{1}$0] and [001] for the (110)-cut DSO and along [100] and [010] for the (001)-cut DSO are shown in Figs. 2(a) and 2(b), respectively. The slight negative values of the extinction coefficients are well within the experimental error bars and do not indicate any amplification or gain in the medium. Evidently, the birefringence between the two in-plane orthogonal axes is larger in the (110)-cut DSO as compared to the (001)-cut DSO over the entire frequency range, see the gray-shaded regions in Figs. 2(a) and 2(b). A waveplate is characterized by the amount of relative phase, δ, that is related to its birefringence, Δn and its thickness d, and it is given by $\delta = 2\pi d\Delta n/\lambda$,

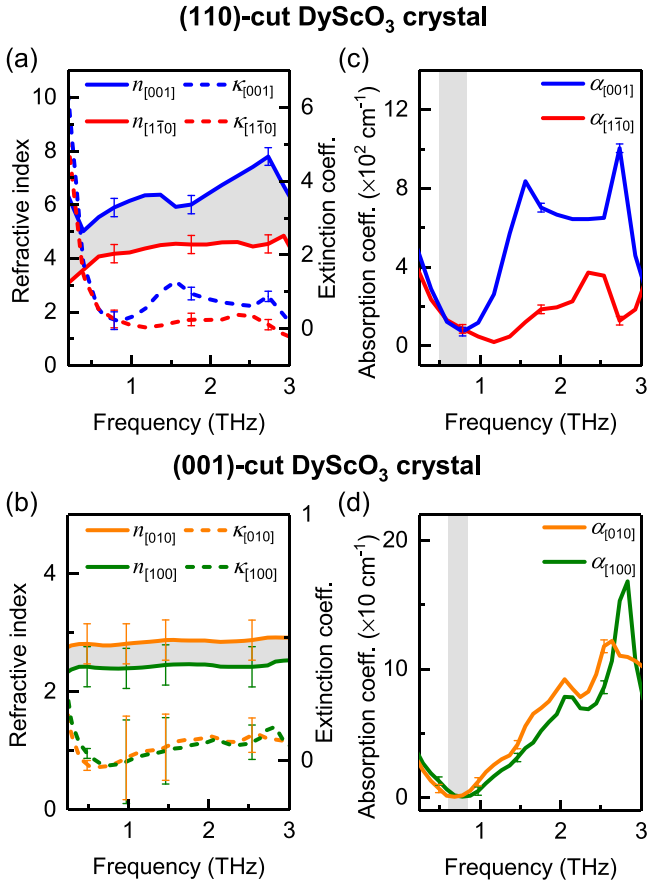

FIG. 2. The frequency-dependent refractive index $\tilde{n}(\omega) = n + i\kappa$ of the DSO crystal for (a) the [001] and [1$\bar{1}$0] axes in the (110)-cut DSO and (b) the [100] and [010] axes in the (001)-cut DSO. The shaded regions indicate the birefringence. (c) and (d) The corresponding absorption coefficients along the respective axes. The shaded regions indicate the frequency range over which the difference in absorption along the two respective in-plane orthogonal axes is negligible.

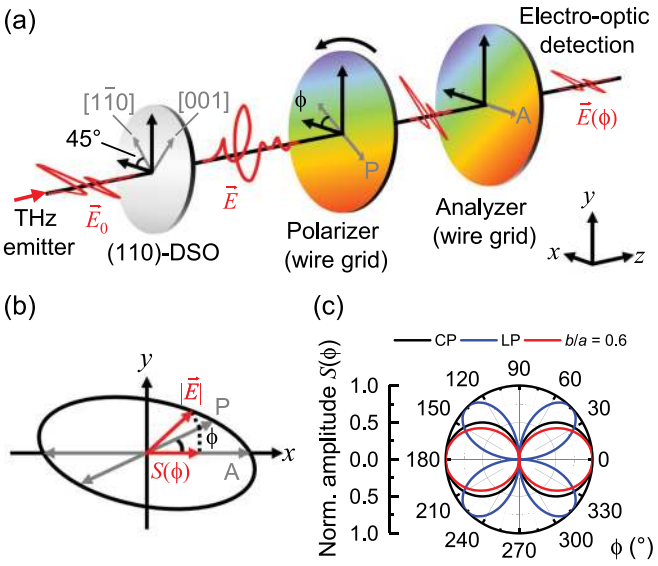

FIG. 3. (a) Schematic of a THz polarimetry setup. (b) Projections of the electric field $\vec{E}$ leading to the measured signal $S(\phi)$. When a linearly-polarized THz radiation, with an electric-field amplitude $\vec{E}_0$, is sent through the DSO crystal oriented at 45° with respect to the x-axis, the transmitted electric field $\vec{E}$ first projects along the polarizer direction (gray, double-sided arrow P) and then along the analyzer direction (gray, double-sided arrow A). ϕ is the rotation angle of the polarizer with respect to the x-axis. The resulting electric field amplitude is given by $S(\phi) = |\vec{E}(\phi)|$. (c) Simulated amplitude, $S(\phi)$, for the circularly-polarized (CP) light, linearly-polarized (LP) light along y-axis and elliptically polarized light ($b/a = 0.6$).

with λ being the wavelength of the THz radiation. We note that the phase retardation goes as $d\Delta n$. This implies that for a crystal with larger birefringence one can use a thinner crystal. Moreover, this justifies the choice of different thicknesses for the two differently oriented DSO crystals. Figures 2(c) and 2(d) show the absorption coefficients for both samples along different crystallographic axes. We find a strong dichroism for both crystals at frequencies above 1 THz. The frequency range of minimal dichroism, see the gray-shaded regions in Figs. 2(c) and 2(d), sets the working frequency range in which the crystal can behave as a zero-order QWP. Evidently, the bandwidth for QWP-like operation is governed by a combination of birefringence and dichroism between the two in-plane orthogonal axes of the DSO crystals.

We use a THz polarimetry technique[32] to map the polarization of the THz pulse modified by the DSO crystal. A simplified schematic of the setup is shown in Fig. 3(a). Here, the x-axis is defined to be parallel to the incident linearly-polarized THz electric field. The [1$\bar{1}$0] axis of the (110)-cut DSO crystal or the [100] axis of the (001)-cut DSO crystal is oriented at an angle of 45° with respect to the x-axis. In this configuration, the transmittances through the (110)-cut DSO and (001)-cut DSO are approximately 30% and 25%, respectively. A set of two linear THz wire grid polarizers are placed right after the DSO crystal. The first polarizer is oriented at an angle ϕ with respect to the x-axis, while the second polarizer, named as analyzer, is fixed along the x-axis. Such an arrangement allows us to determine the phase retardation induced by the DSO crystal without changing the

orientation of the detection crystal. When linearly-polarized THz radiation with an electric field amplitude $\vec{E}_0$ is sent through the DSO crystal, the transmitted electric field $\vec{E}$ can be expressed as $\vec{E} = a\cos(\omega t)\hat{x} + b\cos(\omega t + \delta)\hat{y}$, where a, b, and δ are the ellipticity parameters that directly refer to the retardation and the orientation of the waveplate. Specifically, a and b are linked to the amplitude ratio, while δ is related to the phase retardation of the waveplate.[32] From Fig. 3(b), we see that the transmitted THz wave projects consecutively, first along the polarizer direction (P) and then the analyzer direction (A). Thus, the amplitude $S(\phi)$ of the resulting THz electric field can be expressed as

$$S(\phi) = |\cos\phi|\sqrt{(a\cos\phi + b\sin\phi\cos\delta)^2 + (b\sin\phi\sin\delta)^2}. \quad (1)$$

By measuring $S(\phi)$ as a function of the polarizer angle ϕ, we can obtain the ellipticity parameters of the transmitted THz wave. When the DSO behaves like a QWP that generates CP THz waves, we have $\delta = \pi/2$, $a = b$ and thus Eq. (1) simplifies to $S(\phi) = a|\cos\phi|$, see Fig. 3(c). If the DSO, however, behaves like a half-wave plate, with an incident linearly-polarized light along x-axis, we would get a linearly-polarized light along y-axis. For $\vec{E}$ along the y-axis, we would have $\delta = \pi$, $a = 0$, and Eq. (1) would give $S(\phi) = b/2|\sin 2\phi|$, which is distinctly different. Moreover, for $\delta = \pi/2$ and $a \neq b$, we will have elliptically polarized light. One example is shown as the red curve in Fig. 3(c) with $b/a = 0.6$.

By performing a scan over the full 360° rotation of the polarizer in steps of 10°, we obtain a polar map. Fitting this polar map to Eq. (1), we can obtain the ellipticity parameters of the THz waveform transmitted through the respective DSO crystals. The normalized polar plots of the measured data and fit functions at selected frequencies are shown as dots and solid lines for the (110)-cut DSO and the (001)-cut DSO crystals, respectively, in Figs. 4(a) and 4(b) and Figs. 4(d) and 4(e). The polar plots within the frequency range from 0.5 THz to 0.7 THz, in Figs. 4(a) and (d), show an excellent agreement with the expected results for CP THz light [see black curve in Fig. 3(c)] for both DSO crystals. The fitted results and the deviations are provided in Table I. The phase tolerance limit is within ±3%, while the amplitude ratio, b/a, lies within ±10%. The phase tolerance is defined by the angular acceptance of the retarder, which is approximately ±1.5° at a ±3% change of dephasing. This value is typical for broadband plate retarders as reported earlier in Refs. 32 and 48. A tolerance of ±10% in the amplitude ratio marks the range beyond which

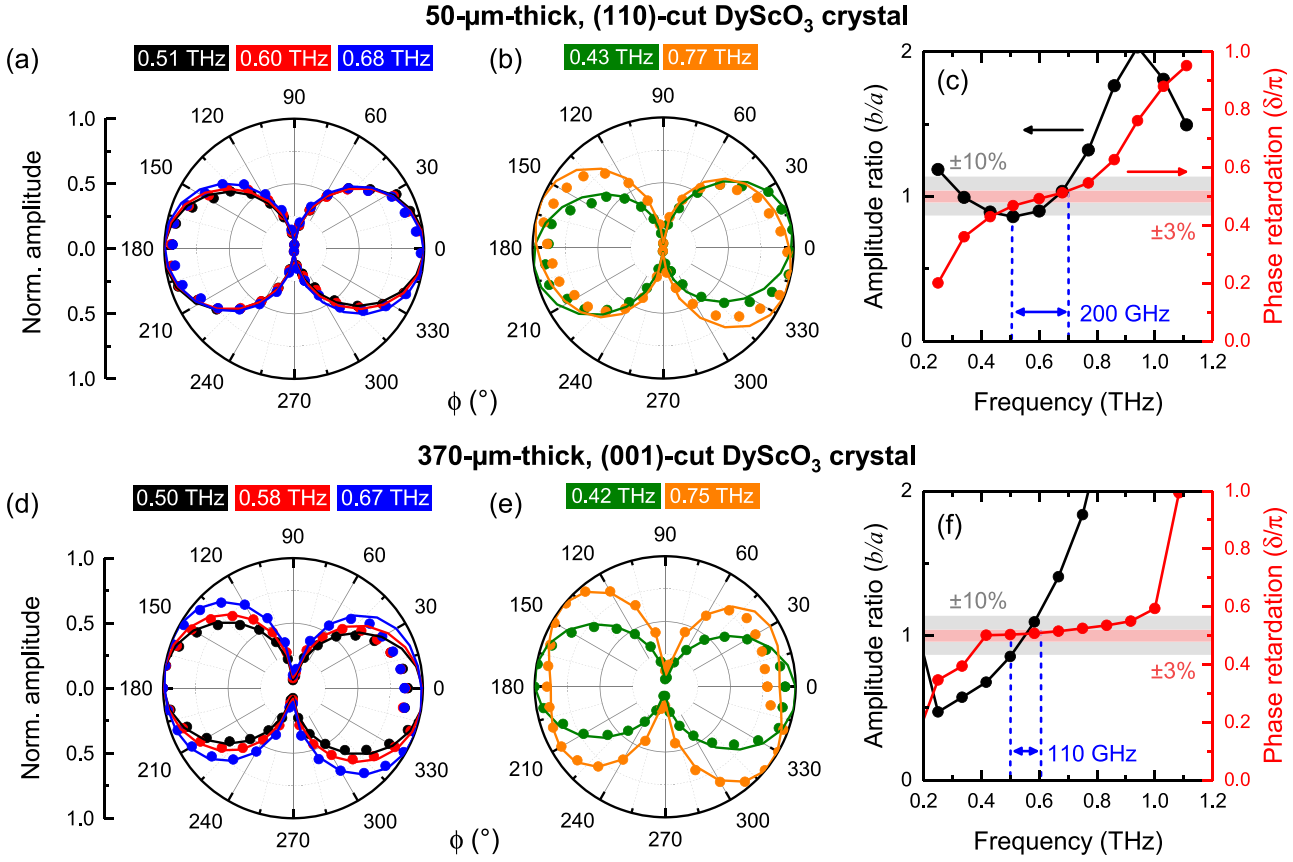

FIG. 4. Polar map of the normalized amplitude $S(\phi)$ at several THz frequencies: (a) 0.51, 0.60, and 0.68 THz and (b) 0.43 and 0.77 THz for the (110)-cut DSO. The filled circles are experimental data, while the solid curves are theoretical fits. (c) The corresponding fitted ellipticity parameters are plotted as a function of frequency. The black curve represents the amplitude ratio between b and a, while the red curve shows the phase retardation δ/π. The blue-dashed lines mark the frequency range where the phase retardation is within a tolerance of ±3% and the amplitude ratio is within a tolerance of ±10%. (d)–(f) Polar maps and the fitted ellipticity parameters for the (001)-cut DSO.

TABLE I. Fitted ellipticity parameters for the THz wave transmitted through the DSO waveplates at different frequencies. Values in brackets show the percentage deviation from an ideal QWP-like performance ($\delta/\pi = 0.5$, $b/a = 1$). The last column shows the standard deviations between the fit and the experimental data.

Sample	Frequency (THz)	δ/π	b/a	Std. dev.
	0.34	0.35 (30)	0.85 (15)	0.16
	0.43	0.45 (10)	0.81 (19)	0.11
	0.51	0.49 (02)	0.80 (20)	0.11
(110)-cut DSO	0.60	0.50 (00)	0.85 (15)	0.12
	0.68	0.51 (02)	0.97 (03)	0.13
	0.77	0.55 (10)	1.23 (23)	0.14
	0.86	0.62 (24)	1.61 (61)	0.17
	0.33	0.39 (22)	0.47 (53)	0.31
	0.42	0.50 (00)	0.58 (42)	0.18
	0.50	0.50 (00)	0.68 (62)	0.15
(001)-cut DSO	0.51	0.50 (00)	0.86 (14)	0.15
	0.67	0.52 (04)	1.09 (09)	0.18
	0.75	0.52 (04)	1.41 (41)	0.20
	0.83	0.53 (06)	1.83 (83)	0.20

the $S(\phi)$ heavily deviates from circular lobes. The polar plots outside the 0.5 THz to 0.7 THz frequency range [see Figs. 4(b) and 4(e)] start to deviate from that of an ideal CP light in either DSO crystals. These deviations of the ellipticity parameters are also manifested on the polar plots in two ways. First, both lobes disorient from the $\phi = 0°$ or 180° polar axes. Second, the shape of the lobes changes from circle to an ellipse. This concomitantly indicates that the phase retardation shifts away from $\pi/2$, and the amplitude ratio diverges from 1 [see Table I for values]. Figures 4(c) and 4(f) show the fitted results of amplitude ratio and phase retardation as a function of frequency for the (110)-cut DSO and the (001)-cut DSO, respectively. The pink- and gray-shaded areas in Figs. 4(c) and 4(f) highlight the phase tolerance of ±3% and the amplitude-ratio tolerance of ±10%, respectively. By satisfying both criteria we find that the effective working frequency range of a single (110)-cut DSO ($\Delta f = 200$ GHz) is three times broader than a single quartz waveplate. Meanwhile, a single (001)-cut DSO also has an effective working frequency range ($\Delta f = 110$ GHz) nearly two times larger than that of a single quartz waveplate. We find that the (110)-cut DSO still outperforms the (001)-cut DSO considering the deviation of ellipticity parameters. In the Poincaré-sphere representation, the polarization state evolves in our DSO waveplate in a single step from linear to circular polarization. This shows our design simplicity in comparison to the six-quartz-plate design that involves multiple polarization state transitions.[32]

In conclusion, we have characterized zero-order THz QWPs made from orthorhombic DSO crystals with two different surface cuts. The refractive indices of the in-plane crystallographic axes in both DSO crystals are measured by the phase-sensitive THz time-domain spectroscopy. With their strong birefringence behaviors, we demonstrate that both the 50-μm-thick (110)-cut DSO and the 370-μm-thick (001)-cut DSO behave like a zero-order THz QWP over a frequency range of 0.5–0.7 THz and 0.50–0.61 THz, respectively, within a ±3% phase and ±10% amplitude-ratio tolerances. Our results expand the possibilities not only for designing a simple achromatic zero-order QWP by combining DSO crystals with different surface cuts, but also for device integration that requires an inherent polarization control of THz light. In addition, because orthorhombic scandates are commonly used as substrates for thin-film technology, our study opens up possible avenues for the investigation of fundamental phenomena in low-dimensional heterostructures that require long wavelength chiral light.

See the supplementary material for detailed analysis and evaluation procedures.

AUTHORS' CONTRIBUTIONS

C.J.Y. and J.Li. contributed equally to this work.

This work was financially supported by the Swiss National Science Foundation via Project Nos. 200021_178825/1 (M.F., J.Li.) and 200021_188414 (M.T.), NCCR MUST via PSP 1-003448-051 (M.F., C.J.Y.), NCCR ETH FAST 3 via PSP 1-003448-054 (M.F., S.P.), ETH via Research Grant No. ETH-28 14–1 (M.F., J.L.), European Research Council via Advanced Grant Program No. 694955-INSEETO (N.S., M.T., M.F.). Further, S.P. acknowledges the support by ETH Career Seed Grant No. SEED-17 18–1.

The authors thank S. Johnson, E. Abreu, and J. Doessegger for providing the THz wire grid polarizers for our polarimetry measurements.

DATA AVAILABILITY

The data that support the findings of this study and the MATLAB evaluation codes are available from the corresponding authors upon reasonable request.

REFERENCES

[1]M. Tonouchi, "Cutting-edge terahertz technology," Nat. Photonics **1**, 97 (2007).
[2]G. P. Williams, "Filling the THz gap–high power sources and applications," Rep. Prog. Phys. **69**, 301 (2006).
[3]S. S. Dhillon, M. S. Vitiello, E. H. Linfield, A. G. Davies, M. C. Hoffmann, J. Booske, C. Paoloni, M. Gensch, P. Weightman, G. P. Williams, E. Castro-Camus, D. R. S. Cumming, F. Simoens, I. Escorcia-Carranza, J. Grant, S. Lucyszyn, M. Kuwata-Gonokami, K. Konishi, M. Koch, C. A. Schmuttenmaer, T. L. Cocker, R. Huber, A. G. Markelz, Z. D. Taylor, V. P. Wallace, J. A. Zeitler, J. Sibik, T. M. Korter, B. Ellison, S. Rea, P. Goldsmith, K. B. Cooper, R. Appleby, D. Pardo, P. G. Huggard, V. Krozer, H. Shams, M. Fice, C. Renaud, A. Seeds, A. Stoehr, M. Naftaly, N. Ridler, R. Clarke, J. E. Cunningham, and M. B. Johnston, "The 2017 terahertz science and technology roadmap," J. Phys. D **50**, 043001 (2017).
[4]K. Reimann, "Table-top sources of ultrashort THz pulses," Rep. Prog. Phys. **70**, 1597 (2007).
[5]R. A. Lewis, "A review of terahertz sources," J. Phys. D **47**, 374001 (2014).
[6]R. Huber, A. Brodschelm, F. Tauser, and A. Leitenstorfer, "Generation and field-resolved detection of femtosecond electromagnetic pulses tunable up to 41 THz," Appl. Phys. Lett. **76**, 3191 (2000).
[7]A. G. Stepanov, J. Kuhl, I. Z. Kozma, E. Riedle, G. Almási, and J. Hebling, "Scaling up the energy of THz pulses created by optical rectification," Opt. Express **13**, 5762 (2005).
[8]M. van Exter, C. Fattinger, and D. Grischkowsky, "Terahertz time-domain spectroscopy of water vapor," Opt. Lett. **14**, 1128 (1989).
[9]D. M. Mittleman, R. H. Jacobsen, R. Neelamani, R. G. Baraniuk, and M. C. Nuss, "Gas sensing using terahertz time-domain spectroscopy," Appl. Phys. B **67**, 379 (1998).

[10]T. D. Dorney, R. G. Baraniuk, and D. M. Mittleman, "Material parameter estimation with terahertz time-domain spectroscopy," J. Opt. Soc. Am. A **18**, 1562 (2001).
[11]P. U. Jepsen and B. M. Fischer, "Dynamic range in terahertz time-domain transmission and reflection spectroscopy," Opt. Lett. **30**, 29 (2005).
[12]G. Folpini, K. Reimann, M. Woerner, T. Elsaesser, J. Hoja, and A. Tkatchenko, "Strong local-field enhancement of the nonlinear soft-mode response in a molecular crystal," Phys. Rev. Lett. **119**, 097404 (2017).
[13]J. Lu, X. Li, H. Y. Hwang, B. K. Ofori-Okai, T. Kurihara, T. Suemoto, and K. A. Nelson, "Coherent two-dimensional terahertz magnetic resonance spectroscopy of collective spin waves," Phys. Rev. Lett. **118**, 207204 (2017).
[14]D. N. Basov, R. D. Averitt, D. van der Marel, M. Dressel, and K. Haule, "Electrodynamics of correlated electron materials," Rev. Mod. Phys. **83**, 471 (2011).
[15]C. Wetli, S. Pal, J. Kroha, K. Kliemt, C. Krellner, O. Stockert, H. v. Löhneysen, and M. Fiebig, "Time-resolved collapse and revival of the Kondo state near a quantum phase transition," Nat. Phys. **14**, 1103 (2018).
[16]S. Pal, C. Wetli, F. Zamani, O. Stockert, H. v Löhneysen, M. Fiebig, and J. Kroha, "Fermi volume evolution and crystal-field excitations in heavy-fermion compounds probed by time-domain terahertz spectroscopy," Phys. Rev. Lett. **122**, 096401 (2019).
[17]P. Kužel, F. Kadlec, and H. Němec, "Dielectric tunability of $SrTiO_3$ thin films in the terahertz range," Appl. Phys. Lett. **88**, 102901 (2006).
[18]N. Strkalj, G. De Luca, M. Campanini, S. Pal, J. Schaab, C. Gattinoni, N. A. Spaldin, M. D. Rossell, M. Fiebig, and M. Trassin, "Depolarizing-field effects in epitaxial capacitor heterostructures," Phys. Rev. Lett. **123**, 147601 (2019).
[19]S. Pal, N. Strkalj, C.-J. Yang, M. C. Weber, M. Trassin, M. Woerner, and M. Fiebig, "Origin of terahertz soft-mode nonlinearities in ferroelectric perovskites," Phys. Rev. X **11**, 021023 (2021).
[20]J. Ji, C. Luo, Y. Rao, F. Ling, and J. Yao, "Investigation of optical pump on dielectric tunability in PZT/PT thin film by THz spectroscopy," Opt. Express **24**, 15212 (2016).
[21]L. Prochaska, X. Li, D. C. MacFarland, A. M. Andrews, M. Bonta, E. F. Bianco, S. Yazdi, W. Schrenk, H. Detz, A. Limbeck, Q. Si, E. Ringe, G. Strasser, J. Kono, and S. Paschen, "Singular charge fluctuations at a magnetic quantum critical point," Science **367**, 285 (2020).
[22]L. A. Nafie, "Infrared and Raman vibrational optical activity: Theoretical and experimental aspects," Annu. Rev. Phys. Chem. **48**, 357 (1997).
[23]S. Spielman, B. Parks, J. Orenstein, D. T. Nemeth, F. Ludwig, J. Clarke, P. Merchant, and D. J. Lew, "Observation of the quasiparticle Hall effect in superconducting $YBa_2Cu_3O_{7-\delta}$," Phys. Rev. Lett. **73**, 1537 (1994).
[24]T. J. Bensky, G. Haeffler, and R. R. Jones, "Ionization of Na Rydberg atoms by subpicosecond quarter-cycle circularly polarized pulses," Phys. Rev. Lett. **79**, 2018 (1997).
[25]J. Wätzel and J. Berakdar, "Open-circuit ultrafast generation of nanoscopic toroidal moments: The swift phase generator," Adv. Quantum Tech. **2**, 1800096 (2019).
[26]P. U. Jepsen, D. G. Cooke, and M. Koch, "Terahertz spectroscopy and imaging–Modern techniques and applications," Laser Photonics Rev. **5**, 124 (2011).
[27]B. Scherger, M. Scheller, N. Vieweg, S. T. Cundiff, and M. Koch, "Paper terahertz wave plates," Opt. Express **19**, 24884 (2011).
[28]Z. Bomzon, G. Biener, V. Kleiner, and E. Hasman, "Space-variant Pancharatnam–Berry phase optical elements with computer-generated subwavelength gratings," Opt. Lett. **27**, 1141 (2002).
[29]G. Li, M. Kang, S. Chen, S. Zhang, E. Y.-B. Pun, K. W. Cheah, and J. Li, "Spin-enabled plasmonic metasurfaces for manipulating orbital angular momentum of light," Nano. Lett. **13**, 4148 (2013).
[30]L. Wang, X.-W. Lin, W. Hu, G.-H. Shao, P. Chen, L.-J. Liang, B.-B. Jin, P.-H. Wu, H. Qian, Y.-N. Lu, X. Liang, Z.-G. Zheng, and Y.-Q. Lu, "Broadband tunable liquid crystal terahertz waveplates driven with porous graphene electrodes," Light Sci. Appl. **4**, e253 (2015).
[31]D. Grischkowsky, S. R. Keiding, M. van Exter, and C. Fattinger, "Far-infrared time-domain spectroscopy with terahertz beams of dielectrics and semiconductors," J. Opt. Soc. Am. B **7**, 2006 (1990).
[32]J.-B. Masson and G. Gallot, "Terahertz achromatic quarter-wave plate," Opt. Lett. **31**, 265 (2006).
[33]G. Komandin, E. Zhukova, V. Torgashev, A. V. Boris, A. A. Boris, E. Motovilova, A. Prokhorov, L. Kadyrov, B. Gorshunov, and M. Dressel, "Terahertz-infrared spectra of the rare-earth scandate $DyScO_3$ single crystal," J. Appl. Phys. **114**, 024102 (2013).
[34]K. J. Choi, M. Biegalski, Y. Li, A. Sharan, J. Schubert, R. Uecker, P. Reiche, Y. Chen, X. Pan, V. Gopalan, L.-Q. Chen, D. G. Schlom, and C. B. Eom, "Enhancement of ferroelectricity in strained $BaTiO_3$ thin films," Science **306**, 1005 (2004).
[35]P. Kužel, F. Kadlec, J. Petzelt, J. Schubert, and G. Panaitov, "Highly tunable $SrTiO_3/DyScO_3$ heterostructures for applications in the terahertz range," Appl. Phys. Lett. **91**, 232911 (2007).
[36]V. Skoromets, C. Kadlec, J. Drahokoupil, J. Schubert, J. Hlinka, and P. Kužel, "Systematic study of terahertz response of $SrTiO_3$ based heterostructures: Influence of strain, temperature, and electric field," Phys. Rev. B **89**, 214116 (2014).
[37]L. Baldassarre, A. Perucchi, S. Lupi, and P. Dore, "Far infrared properties of the rare-earth scandate $DyScO_3$," J. Phys.: Condens. Matter **22**, 355402 (2010).
[38]P. Kühne, C. M. Herzinger, M. Schubert, J. A. Woollam, and T. Hofmann, "An integrated mid-infrared, far-infrared, and terahertz optical Hall effect instrument," Rev. Sci. Instrum. **85**, 071301 (2014).
[39]D. Peev, T. Hofmann, N. Kananizadeh, S. Beeram, E. Rodriguez, S. Wimer, K. B. Rodenhausen, C. M. Herzinger, T. Kasputis, E. Pfaunmiller, A. Nguyen, R. Korlacki, A. Pannier, Y. Li, E. Schubert, D. Hage, and M. Schubert, "Anisotropic contrast optical microscope," Rev. Sci. Instrum. **87**, 113701 (2016).
[40]P. Kühne, N. Armakavicius, V. Stanishev, C. M. Herzinger, M. Schubert, and V. Darakchieva, "Advanced terahertz frequency-domain ellipsometry instrumentation for *in situ* and *ex situ* applications," IEEE Trans. Terahertz Sci. Technol. **8**, 257 (2018).
[41]P. Gopalan, S. Knight, A. Chanana, M. Stokey, P. Ranga, M. A. Scarpulla, S. Krishnamoorthy, V. Darakchieva, Z. Galazka, K. Irmscher, A. Fiedler, S. Blair, M. Schubert, and B. Sensale-Rodriguez, "The anisotropic quasi-static permittivity of single-crystal β-Ga_2O_3 measured by terahertz spectroscopy," Appl. Phys. Lett. **117**, 252103 (2020).
[42]C. M. Morris, R. V. Aguilar, A. V. Stier, and N. P. Armitage, "Polarization modulation time-domain terahertz polarimetry," Opt. Express **20**, 12303 (2012).
[43]M. Neshat and N. P. Armitage, "Developments in THz range ellipsometry," J. Infrared, Millimeter, Terahertz Waves **34**, 682 (2013).
[44]L. Wu, A. Farid, N. J. Laurita, T. Mueller, and N. P. Armitage, "A compact broadband terahertz range quarter-wave plate," J. Infrared, Millimeter, Terahertz Waves **41**, 642 (2020).
[45]K. Xu, E. Bayati, K. Oguchi, S. Watanabe, D. P. Winebrenner, and M. Hassan Arbab, "Terahertz time-domain polarimetry (THz-TDP) based on the spinning E-O sampling technique: determination of precision and calibration," Opt. Express **28**, 13482 (2020).
[46]C.-J. Yang, S. Pal, F. Zamani, K. Kliemt, C. Krellner, O. Stockert, H. v Löhneysen, J. Kroha, and M. Fiebig, "Terahertz conductivity of heavy-fermion systems from time-resolved spectroscopy," Phys. Rev. Res. **2**, 033296 (2020).
[47]W. Withayachumnankul and M. Naftaly, "Fundamentals of measurement in terahertz time-domain spectroscopy," J. Infrared, Millimeter, Terahertz Waves **35**, 610 (2014).
[48]J. M. Beckers, "Achromatic linear retarders with increased angular aperture," Appl. Opt. **11**, 681 (1972).